Modeling and System Identification of a Life-Size Brake-Actuated Manipulator

Brian Dellon and Yoky Matsuoka, *Member, IEEE*

***Abstract*—Safety is a critical factor when designing a robotic rehabilitation environment. Whole-limb or life-size haptic interaction would allow virtual robotic rehabilitation of daily living activities such as sweeping or shelving. However, it has been too dangerous to implement such an environment with conventional active robots that use motor, hydraulic, or pneumatic actuation. To address this issue, a life-size 6-degree-of-freedom (DOF) brake-actuated manipulator (BAM) was designed and constructed. This paper details the BAM's system models including mechanisms, kinematics, and dynamics, as well as detailed input and friction models. In addition, a new system-identification technique that utilizes human input to excite the robot's dynamics with unscented Kalman filtering was employed to identify system parameters. Noise sources are discussed, and the model is validated through force estimation with inverse dynamics. Model parameters and performance are compared with other commercially available haptic devices. The BAM shows a significantly larger workspace, maximum force, and stiffness over other devices exhibiting its promise toward rehabilitative applications.**

***Index Terms*—Brake-actuated manipulator (BAM), passive haptic, robotic rehabilitation, system identification, unscented Kalman filter.**

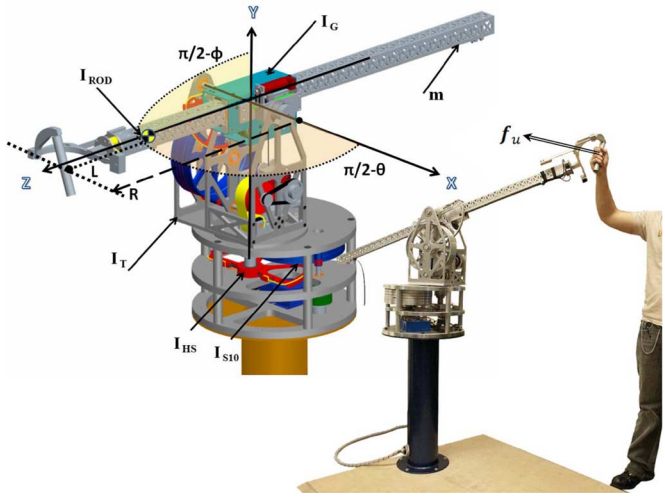

Fig. 1. BAM, annotated with pertinent inertias and dimensions. Inertias I_{hs} and I_{s10} are part of the cable drive transmission and are elements in both pitch and yaw. $I_{\rm rod}$ is the inertia tensor for the robots prismatic joint, and I_g is the inertia of the arm's guide box containing the prismatic joint's particle brake.

I. Introduction

GENERAL-PURPOSE haptic devices are commonly used as an assistive technology to enhance a human's interaction within a virtual framework, whether it is performing a surgical procedure (virtual fixtures), designing a car (virtual clay), training a sports technique, or rehabilitation. A haptic display, by definition, requires physical human–robot interaction (pHRI), and the moment when the robot and a human contact intimately, the safety of the user must be considered. So far, commercially available haptic devices have either limited their workspace to minimize safety concerns (Phantom [1], Delta Haptic Device (DHD) [2]) or utilized software safety mechanisms to augment larger inertia and energetic mechanical components (whole arm manipulator (WAM) [3], haptic master [4]).

The field of haptic devices has reached a maturity where the future directions include domestic rehabilitation with users who are weak, disabled, or have a hard time coordinating their limbs. In other applications, such as video games, the users may be highly physical and strong and, hence, will push the limits of the device in their home. In these situations, having a large pHRI environment with energetic or high-inertial systems and solely software safety is no longer sufficient. The preliminary work in the realm of research has shown the utility of large pHRI environment for rehabilitation [5], [6], and it is the time to assure that we can construct and explore the ability and limitations of large pHRI systems without energetic or high-inertial loads. One approach toward this problem is to construct and analyze a brake-actuated haptic environment.

A brake-actuated haptic device falls into a specific category of passive devices. There are two main classes of passive device: steerable and dissipative. The main difference is in the method of actuation. Steerable devices, such as a Cobot [7], use a continuously variable transmission to reorient their degrees of freedom, but their force output depends largely on the amount of friction at its interface and can be mechanically complex. The second class uses either brakes or clutches to dissipate or redirect energy in the required direction. Dissipative devices are inherently stable and mechanically simple; an example of this type is the planar-trajectory-enhancing robot (PTER) [8], which employed a planar workspace to demonstrate its properties and path following abilities.

In this paper, we present a 6-degree-of-freedom (DOF) dissipative haptic device called the brake-actuated manipulator (BAM), as shown in Fig. 1. The original theoretical kinematic

Manuscript received September 21, 2008; revised February 6, 2009. First published April 24, 2009; current version published June 5, 2009. This paper was recommended for publication by Associate Editor M. Johnson and Editor K. Lynch upon evaluation of the reviewers' comments. This work was supported in part by the National Science Foundation under Grant 0238204 and in part by the National Institutes of Health under Grant R21HD47405.

B. Dellon is with the Department of Mechanical Engineering, Carnegie Mellon University, Pittsburgh, PA 15213 USA (e-mail: btd@andrew.cmu.edu).

Y. Matsuoka is with the Department of Computer Science, University of Washington, Seattle, WA 98195 USA (e-mail: yoky@cs.washington.edu).

Color versions of one or more of the figures in this paper are available online at http://ieeexplore.ieee.org.

Digital Object Identifier 10.1109/TRO.2009.2017804

analysis is presented in [9]. Brakes were selected for actuation to dramatically increase the size of the workspace using their high energy density and controllability. A brake-actuated large haptic environment is suitable for rehabilitation as it has programmable resistive forces without any potential of moving on its own to strike users. This haptic device's mechanism, kinematics, and dynamics are presented in Section II. Before the device could actually be used for rehabilitation paradigms, the device's full model parameters must be identified and validated for accurate control. Here, we present a new system identification technique that allows human input to excite the robot's dynamics in Section III. Using this technique, identified model parameters are shown in Section IV, and validated through an inverse dynamic analysis in Section V. At the end of the paper, these parameters and performance are discussed and compared with other commercially available haptic devices to show the BAM's superiority toward larger rehabilitation applications.

II. Modeling

A. Mechanisms

The BAM (see Fig. 1) is a 6-DOF dissipative force feedback haptic robot, designed for whole-body rehabilitation and experimentation on the human musculoskeletal system through the simulation of virtual environments. The device is composed of three main components, a base that houses the cable drive for the yaw axis, a turret section that sits atop the base and swivels to provide yaw motion and houses the cable drive for the pitch axis, and finally, the prismatic joint is located at the top of the turret and can be pitched up and down while providing a stage for extension. The main spherical axes (pitch, yaw, and extension) are actuated by magnetorheological (MR) particle brakes, while the additional 3 DOF at the handle are unactuated. Here, we will ignore all effects (except mass) from the three unactuated handle axes. The MR brakes drive tensioned cable transmissions for each rotary joint (yaw and pitch), and the prismatic joint (extension) has a timing belt drive. The BAM employs a novel hybrid gravity compensator to hold the weight of the prismatic joint, even at its full extension of 1 m. The gravity compensator is composed of a lead screw and carriage assembly that transmits the gravity torque to the prismatic joint. Each subsystem requires a particular model; we begin by defining the kinematics.

B. Kinematics

It has been shown that a passively actuated robot must have orthogonal kinematics to control all the forces in the Cartesian space of the user [9]. To demonstrate this, we set the robot's kinematics $\vec{q}$ so that the end-effector opposes an externally imposed motion and constrain the joints to dissipate energy, satisfying passivity

$$\boldsymbol{v}^T \boldsymbol{f} = \boldsymbol{v}^T(-C\boldsymbol{v}) = -\boldsymbol{v}^T C\boldsymbol{v} \leq 0 \tag{1}$$

$$\dot{q}_i \tau_i \leq 0 \tag{2}$$

where $\boldsymbol{v}$ is the end-effector velocity vector, $\boldsymbol{f}$ is the resistive force opposing the user's motion, $\dot{q}_i$ and τ_i are the *i*th joint's angular velocity and torque, and *C* is a damping matrix. Expanding the passivity constraint (2) at each joint under the conditions of (1) leads to

$$\begin{aligned}\dot{q}_i \tau_i &= \dot{q}_i (J^T \boldsymbol{f})_i = \dot{q}_i (J^T(-C\boldsymbol{v})_i = \dot{q}_i j_i^T(-CJ\dot{\boldsymbol{q}})) \\ &= -\dot{q}_i j_i^T C \sum_j^n j_j \dot{q}_j \leq 0\end{aligned} \tag{3}$$

for all *n* joints of the robot, where j_j is the *j*th row of the Jacobian. If we further assume orthogonal kinematics, (3) becomes

$$\dot{q}_i \tau_i = -\dot{q}_i j_i^T C \sum_j^n j_j \dot{q}_j = -\dot{q}_i^2 j_i^T C j_i \leq 0. \tag{4}$$

Therefore, a robotic arm with any number of possible orthogonal kinematics can resist an externally imposed motion with brakes. If a typical fully revolute kinematic design was chosen, (3) would not collapse into (4), but rather expand to incorporate independent torques generated from motion of other joints as well. The expansion of (3) for revolute designs leads to conditions where joint velocities necessary to oppose an external force will violate the passivity constraint (2). Consequently, the BAM's kinematics are spherical, not only to fulfill the requirement posited by [9] but to reduce inertia by incorporating as few prismatic stages as possible while maintaining kinematic orthogonality as well.

An inertial frame of reference is set at the kinematic center of the device, where the yaw pitch and extension axes intersect; this point is the origin of Cartesian space, as depicted in Fig. 1. First, the generalized coordinates for the device are set as

$$\vec{q} = [\theta(t)\phi(t)r(t)]^T \tag{5}$$

where θ is the yaw, ϕ is the pitch, and *r* is the extension of the prismatic joint measured to the handle's grip. The parameterization of time will, henceforth, be omitted in the following equations. It can be shown for our spherical device that the transformation into Cartesian coordinates $\vec{X}$, and its corresponding Jacobian *J* are then described by

$$\vec{X} = \begin{bmatrix} (r-L)\cos(\phi)\sin(\theta) \\ (r-L)\sin(\phi) \\ (r-L)\cos(\phi)\cos(\theta) \end{bmatrix} \tag{6}$$

$$J = \frac{d\vec{X}}{d\,\vec{q}} \tag{7}$$

where $\vec{X} = [x\ y\ z]^T$, and *L* is the distance from the handle's grip to the prismatic joint's center of gravity. The attitude matrix *A* is constructed for the purpose of transforming a vector given in a coordinate system rotated relative to the reference frame into the latter. The attitude is defined by Euler angles for a rotation about θ and then ϕ. The attitude matrix also defines a skew-symmetric matrix given by $[\![\sim\omega]\!]$, which is related to the angular velocity

of the prismatic joint $\vec{\omega}_{\mathrm{rod}}$; thus

$$\dot{A}A^{-1} = \begin{bmatrix} 0 & -\omega_{z,\mathrm{rod}} & \omega_{y,\mathrm{rod}} \\ \omega_{z,\mathrm{rod}} & 0 & -\omega_{x,\mathrm{rod}} \\ -\omega_{y,\mathrm{rod}} & \omega_{x,\mathrm{rod}} & 0 \end{bmatrix}. \tag{8}$$

C. Dynamics

Lagrangian mechanics can be used to describe the motion of a wide variety of dynamic systems. To derive the equations of motion for the BAM, we first consider the robot's kinetic and potential energies defined as follows:

$$\mathrm{PE} = m_{\mathrm{rod}} g(r - L)\sin(\phi) \tag{9}$$

$$\begin{aligned}\mathrm{KE} = {} & \frac{1}{2}(m_{\mathrm{rod}} \dot{\vec{X}}^T \dot{\vec{X}} + \frac{1}{2}\vec{\omega}_{\mathrm{rod}}^{\,T} l_{\mathrm{rod}} \vec{\omega}_{\mathrm{rod}} \\ & + (l_g + I_{hs} + I_{s10}N^2)\dot{\phi}^2 \\ & + (l_t + I_{hs} + I_{s10}N^2)\dot{\theta}^2)\end{aligned} \tag{10}$$

where I_{rod} is the inertia tensor for the prismatic joint at its center of gravity, I_g is the rotational inertia of the prismatic joint guide box, I_t represents the turret section's inertia, I_{hs} is the inertia for the low-speed section of the cable drive, I_{s10} is the inertia for the high-speed reducer in the cable drive, and N is the velocity ratio between the low- and high-speed sections. These inertias are depicted in Fig. 1. Next, the Lagrangian is calculated by subtracting (9) from (10)

$$L = \mathrm{KE} - \mathrm{PE}. \tag{11}$$

The equations of motion are initially found using Lagrange's equation without any working wrenches

$$\Lambda = \frac{d}{dt}\left(\frac{\partial L}{\partial \dot{\vec{q}}}\right) - \frac{\partial L}{\partial \vec{q}} = 0 \tag{12}$$

and the mass matrix M is constructed by taking the second derivative of the kinetic energy (10) with respect to the time derivative of the generalized coordinates

$$M_{ij} = \frac{\partial^2 KE}{\partial \dot{q}_i \partial \dot{q}_j}, \qquad (i, j = 1, \ldots, 3). \tag{13}$$

To finalize the equations of motion, we put it in a standard form by solving for $\ddot{q}_l$. This is accomplished by setting the second-order terms of Λ from (12) to zero, applying any conservative forces acting on the system, and then multiplying by the inverse of M

$$\begin{aligned}\ddot{\vec{q}} &= f(\vec{q}, \dot{\vec{q}}, \vec{u}, \vec{t}) \\ &= M^{-1}(-\Lambda|_{\ddot{\vec{q}}=0} - \vec{\tau}_{\mathrm{friction}} + \vec{\tau}_{\mathrm{input}}).\end{aligned} \tag{14}$$

D. Input Models

The inputs to the system are composed of three orthogonal forces on the handle's grip supplied by the user, measured relative to the endpoint of the prismatic joint, three braking torques to produce virtual constraints, and gravity compensation torque/forces about the pitch axis from the gravity compensator (see Fig. 2) and along the extension axis provided by the brakes. First, we discuss the external mechanism used to provide gravity compensation at about ϕ and then describe the behavior of our MR actuators. Finally, we calculate the effect of user input at the joint level.

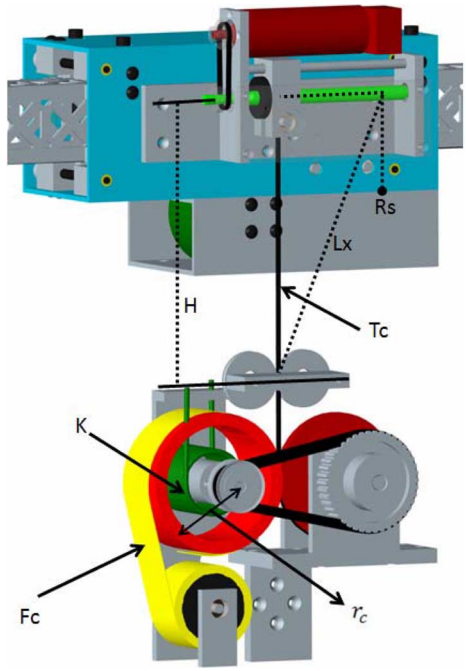

Fig. 2. Cutaway of the pitch axis gravity compensation mechanism. A constant force spring (Fc) in parallel with a torsion spring (K) supplies the necessary torque to counter gravity. The torque is adjusted by driving a carriage's position (Rs) on the lead screw proportional to the extension of the prismatic joint.

1) Gravity Compensation: The gravity compensation mechanism depicted in Fig. 2 is considered quasi-static because the gear train has very low inertia compared with the bulk of the device, and the components rotate only over a fraction of a radian (slowly), even for large movements.

The geometry of the gravity compensator is chosen so that a linear spring can be used to exactly counter the weight of the pitch axis independent of ϕ [10]. The basic geometry is defined by the triangle composed of lengths "Rs," "H," and "Lx," as seen is Fig. 2. Length "Lx" changes with rotation about ϕ for a given "Rs," because this length is coupled with the main spring through a gearing Δ, and it will stretch the main spring producing force "Tc" in the cable acting at "Rs." Total compensating torque changes based on the cable's tension and moment arm about ϕ. With this configuration, as "Tc" increases (from increasing "Lx"), the moment arm decreases, proportionally maintaining a constant torque. However, due to the prismatic joint, the total gravity torque can vary depending on the degree of extension. Hence, our implementation adds prismatic functionality by augmenting the geometry through a lead screw and carriage driven by a small dc motor. Note, the tensioned cable is connected to the carriage and thus can be actuated along "Rs." If the carriage is driven to a position "Rs" proportional to the excursion of the prismatic joint's center of gravity by a constant

"c," then the necessary torsional spring constant to maintain static balance will be

$$K = \frac{mgc}{H\Delta^2} \tag{15}$$

where m is the mass of the arm, H is the distance depicted in Fig. 2, and Δ is the gearing from the spring torque to the force in the tensioned cable "Tc." Since the motor moves the carriage almost perpendicular to the cable, only a fraction of the motor energy can be conveyed to the user, and safety is maintained. Analyzing the triangle created by "Rs," "H," and "Lx" with the law of cosines and other trigonometric identities and then performing static balance on this device reveals the gravity compensation torque to be

$$\begin{aligned} Rs &= \frac{(r-L)}{c} \\ Lx &= \sqrt{Rs^2 + H^2 - 2RsH\,\sin(\phi)} \\ L_0 &= \frac{r_c Fc}{K\Delta} \\ Tc &= (r_c Fc + K(Lx - L_0)\Delta)\Delta \\ \tau_{gc,\phi} &= \frac{TcHRs\,\cos(\phi)}{Lx}. \end{aligned} \tag{16}$$

The gravity-compensator torque described by (16) might seem to have a dependence on both r and ϕ, but when the loading function $mg(r-L)\cos(\phi)$ is taken into account, it becomes apparent that a linear spring can be utilized. The magnitude of the constant force spring term Fc is chosen to create a zero initial spring length for the main torsional spring. Choosing Fc in this way not only preloads the compensator but also decreases the required torsion spring deflection, reducing the effects of fatigue.

Currently, only partial gravity compensation can be achieved along r using the MR brakes without an external mechanism, as depicted in Fig. 2. In this scheme, gravity canceling forces are only generated if $\dot{r}\phi \leq 0$; otherwise, the user receives no assistive force

$$f_{gc,r} = \begin{cases} mg\,\sin(\phi), & \dot{r}\phi \leq 0 \\ 0, & \dot{r}\phi > 0. \end{cases} \tag{17}$$

2) MR Particle Brake Model: MR fluids are colloidal suspensions of ferrous particles whose rheological properties change rapidly when exposed to magnetic fields. The use of fluids enables the brake to have a fast response time, and produce torque independent of angular velocity and proportional to input current [11]. An MR particle brake is in essence a friction device, and is modeled as a programmable Coulomb friction element in [12]. We apply the same Coulomb modeling technique but include the effect of saturation. This saturation captures the static friction produced from the brakes by canceling out joint torques. The braking torques are defined as

$$\tau_{\mathrm{brake},i} = \begin{cases} \mathrm{sign}(\dot{q}_i)\tau_{\mathrm{set},i}, & |\tau_{\mathrm{joint},i}| > \tau_{\mathrm{set},i} \\ \tau_{\mathrm{joint},i}, & |\tau_{\mathrm{joint},i}| \leq \tau_{\mathrm{set},i} \end{cases} \tag{18}$$

where $\tau_{\mathrm{set},i}$ is the commanded torque level for the brake belonging to joint i, and $\tau_{\mathrm{joint},i}$ is the total torque acting on joint

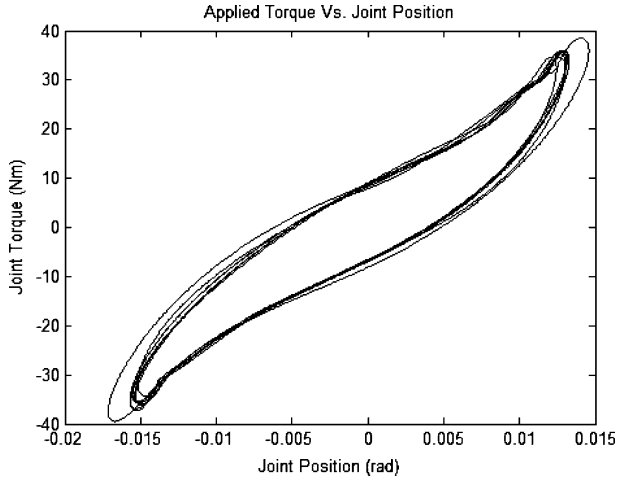

Fig. 3. Typical hysteresis loop observed for the yaw-axis cable drive transmission.

"i," including gravity. In addition sign() is the signum function defined to be zero when $\dot{q}_i$ is zero. With the brake model defined in this way, the brakes are able to "lock" or restrain a particular degree of freedom when $\tau_{\mathrm{set},i}$ is large compared to $\tau_{\mathrm{joint},i}$. Any passive frictional effects from the brakes that are not generated from a magnetic flux through the rheological material are taken into account in (20).

3) Torque Component From Human Input: In operation, the user's input forces are orthogonal to the orientation of the prismatic joint; therefore, they must be transformed into the reference frame using an attitude matrix A. Applying the Jacobian from (7), we can determine the resulting joint torque components from the user

$$\vec{\tau}_{\,\mathrm{user}} = J^T A\,\vec{f}_{\,\mathrm{user}}. \tag{19}$$

E. Transmission and Friction Models

The BAM contains two styles of transmission, a pretensioned linear belt drive for the prismatic joint and a pretensioned cable capstans for the pitch and yaw axes. Cable drives have many desirable properties for a transparent haptic interface because they can be back-drivable, possess low friction, zero backlash, and high stiffness per unit length for a small mass [13]. In order to model such transmissions, we first make some assumptions. The cable is assumed to be weightless and incapable of slipping during usage. In addition, it is assumed that all frictional effects are proportional to the amount of pretension in the drive. Under these assumptions, we can check to see if the transmissions are stiff enough to be considered rigid for dynamic purposes.

Stiffness is measured by commanding $\tau_{\mathrm{set},i}$ to its maximum value, this locks each axis of the device in place. The joints are loaded manually, force measurements are recorded from the handle, and joint deviations from the center are measured. This processes produces hysteresis loops, one such loop for the yaw axis is shown in Fig. 3 using smoothed force and position data. The resulting stiffness for all three axes is presented in Table I.

TABLE I
TRANSMISSION STIFFNESS VALUES

Parameter	Magnitude	Standard Deviation
K_θ	2.3 kNm/rad	0.013 kNm/rad
K_ϕ	2.1 kNm/rad	0.009 kNm/rad
K_r	109 kN/m	0.694 kN/m

TABLE II
PARAMETERS EXTRACTED FROM CAD

Parameter	Magnitude
L	0.461 m
m	3.56 kg
I_g	28.8 gm^2
I_{hs}	4.313 gm^2
I_{s10}	15.52 gm^2
I_t	187 gm^2
I_{rod}	$\begin{bmatrix} 821 & -0.801 & 0.783 \\ -0.801 & 826 & 0.052 \\ 0.783 & 0.052 & 10.25 \end{bmatrix}$ gm^2

The inertia terms in (9) and (10) have been calculated with a CAD software package based on the detailed 3-D models created for the design of the BAM. These values include weights of minutia such as nuts, bolts, cables, and timing belts. The inertia estimates have been found to be in excellent agreement (within human margin of error) when compared with physical measurements taken of actual weight and center of mass using a string balance; this result helps validate our CAD values. The inertias used in the following experiments are shown in Table II.

Calculating the inertia matrix from (13) for values at maximum prismatic extension, we get each transmission's bandwidth. For the yaw and pitch axes, their bandwidth is approximately 25 Hz, and the prismatic joint is close to 175 Hz. Because the identification process will be using low input bandwidth ranging 0.1–2 Hz, we can consider both types of transmissions to be rigid and have treated them as such for solving the dynamics.

Friction modeling is important in a haptic device, especially identifying nonlinear effects that occur during low-velocity movements. Various static and dynamic friction models, such as Coulomb friction, stiction, frictional lag, and the Stribeck effect, often have seven or more parameters associated with them [14]. Regardless of a motor actuated device's ability to accurately identify its frictional characteristics [15], haptic devices often use a simple static model, as shown in [16] and [17]. Because the Gaussian random variables in the unscented Kalman filter, which are used here for system identification, capture the frictional complexity as a degree of model uncertainty, nonlinear effects are not explicitly modeled; therefore, we use a simple viscous coulomb model defined by

$$\vec{\tau}_{\text{friction}} = K_d \dot{\vec{q}} + Fc\,\text{sign}(\dot{\vec{q}}) \tag{20}$$

where K_d is a diagonal matrix of damping coefficients and Fc is a diagonal matrix of Coulombic friction terms. These static and dynamic friction values are meant to be holistic, representing total joint friction including any passive frictional effects generated at the brakes and felt through the transmission. It is assumed that the damping and friction elements are independent for each axis. In order to validate the viscous Coulomb friction model for the BAM, we examine the difference between estimated user forces from the inverse dynamic model *without friction terms* against measured force input. This difference is an indication of the underlying frictional characteristics. Fig. 4 displays a typical hysteretic friction curve obtained for the yaw axis, and shows the estimated and measured force input. The friction curve displays distinct viscous Coulomb behavior in the deceleration phase of the given motion. This implies that the simple friction model (20) is sufficient, assuming we ignore the hysteresis effects.

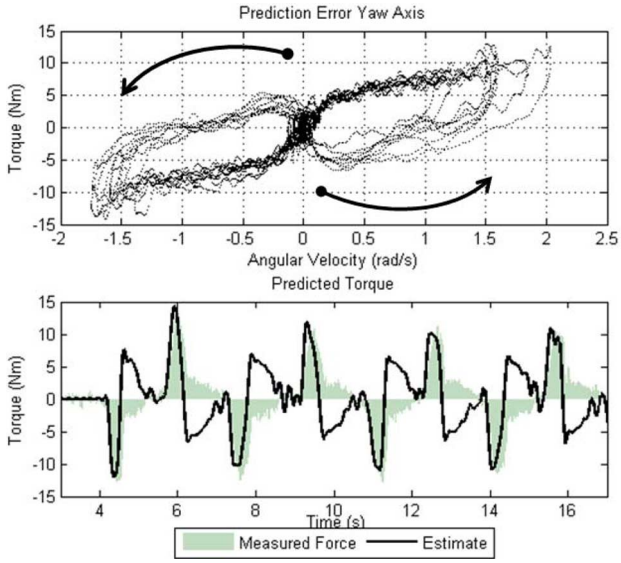

Fig. 4. (Top) Prediction error for the inverse dynamic model without friction terms; arrows indicate path of initial acceleration. (Bottom) Corresponding measured and estimated torque impulses for a single trial. Without friction the torque estimate overshoots zero.

III. SYSTEM IDENTIFICATION OF PASSIVE MECHANISMS

A. Background

System identification of a passive mechanism is critical; without accurate system parameters, there would be a discrepancy between what a user feels and what is meant to be experienced through a virtual environment. These discrepancies are realized through the device's apparent inertia, friction, and stiffness. System properties must be fully understood in order to apply proper control laws.

One implication of using brakes for actuation is that the robot becomes "under-actuated," or energetically passive. The consequence of this fact is that system identification cannot be performed in the standard way, which is to use input motor torques to provide unique movement trajectories to maximally excite the system parameters [16]–[18]. This makes system identification a challenge that would otherwise not exist for active devices. For simplicity, we use human input to excite the system dynamics instead of an external forcing pendulum or other device.

We show that human input is sufficient to calculate an accurate estimate of the system characteristics.

System identification of multidegree of freedom devices often requires specialized modeling and statistical techniques. A common form applies least squares optimization on the equations of motion describing the system [16], [19]. In order to deal with multijoint estimation, one group performed a nonlinear optimization with a joint "locking" scheme to decouple the equations of motion for each axis of the Freedom 6S (MPB Technologies, Canada) [20], which effectively decreases the number of parameter estimates for each joint while ignoring interaction torques between joints. Unfortunately, the validity of least squares estimate depends highly on the quality of the signals and whether the input trajectories can excite all of the robot dynamics [18]. Other nonparametric techniques such as neural nets and support vector machines have been employed [21], [22] but lack the physical grounding and insight that a parameterized estimation process can give.

Kalman filtering is a popular approach to fuse multiple noisy sensor signals for prediction based on hidden Markov models and recursive Bayesian estimation. The extended Kalman Filter (EKF) has been used to solve a constrained nonlinear dynamic system for both its states and surface constraint parameters using noisy force sensor measurements [23]. While the EKF has its benefits over other techniques mentioned before, large errors can be introduced in the mean and covariance of the random variable due to linearization of the dynamics [24], [25]. The unscented Kalman filter (UKF) can overcome the problems of the EKF due to its deterministic sampling approach whereby samples from the random variables are propagated through the true nonlinear dynamics, preserving the mean and covariance. Specific advantages of the UKF include the following:

1) lower expected error than EKF;
2) applicability to nondifferentiable functions;
3) circumvents linearization of the dynamics;
4) robustness toward initial conditions;
5) incorporation of model uncertainty.

B. State and Parameter Estimation

The UKF works on the premise that with a deterministic sampling from a random variable, it should be easier to approximate a Gaussian distribution than to approximate an arbitrary nonlinear function through linearization. A full derivation of the UKF and details of its implementation can be found in [25]. The true system model is given in discrete time by

$$\begin{aligned} \vec{x}_{k+1} &= f(\vec{x}_k, \vec{w}_k, \vec{u}, k), \qquad \vec{w}_k \sim N(\vec{0}, Q_k) \\ \tilde{\vec{y}}_k &= h(\vec{x}_k, \vec{v}_k, \vec{u}, k), \qquad \vec{v}_k \sim N(\vec{0}, R_k) \end{aligned} \tag{21}$$

where the quantity $\vec{\omega}_k$ is the process noise on the system of differential equations that can be tuned to compensate for model inaccuracy and control filter convergence, $\tilde{\vec{y}}_k$ is the sensor measurement model, and the function h(..) returns a 6×1 stacked vector of position and velocity. The measurement noise $\vec{v}_k$ represents the inherent noise in the sensor signals, and $\vec{u}$ is the sum total of all system inputs. The variables $\vec{v}_k$ and $\vec{w}_k$ are assumed to be zero-mean Gaussian white noise processes; this preserves the diagonal structure of the error covariance matrix. A Markov assumption is also made to facilitate recursive estimation. Under the Markov assumption, the values in any state are influenced only by the values of the state that directly preceded it.

TABLE III
EXPANDED STATE MATRIX FOR UNSCENTED KALMAN FILTER

$x(1) = \theta$	$x(5) = \phi$	$x(9) = r$
$x(2) = K_{d\theta}$	$x(6) = K_{d\phi}$	$x(10) = K_{dr}$
$x(3) = F_{c\theta}$	$x(7) = F_{c\phi}$	$x(11) = F_{cr}$
$x(4) = \dot{\theta}$	$x(8) = \dot{\phi}$	$x(12) = \dot{r}$
	$x(13) = m$	

A new augmented state vector $\vec{x}_k$ is introduced in (21). This vector contains the states of a set of first-order nonlinear differential equations converted from the dynamic model in (14), and additional states for parameter estimation. The variable $\dot{\vec{x}}_k$ for each model parameter is set equal to zero, and the parameter state is allowed to vary in a "random walk" process. The noise terms $\vec{v}_k$ and $\vec{w}_k$ are also concatenated into $\vec{x}_k$ since the noise is not linearly additive. The full state matrix without additional noise states is shown in Table III.

As a next step, the nonlinear and continuous time equations of motion from (14) must be converted to a discrete time version that is compatible with the measurement and system models from (21). To do so, we use a Runge Kutta method to solve the initial value problem and obtain the state at the next time step by dividing the time interval into "n" smaller steps of size δ

$$\begin{aligned} \dot{\vec{x}} &= f(\vec{x}, \vec{u}, \vec{t}), \vec{x}(t_0) = \vec{x}_0 \\ k_1 &= f(\vec{x}_k, \vec{u}_k, \vec{t}_k) \\ k_2 &= f\left(\vec{x}_k + k_1 \frac{\delta}{2}, \vec{u}_k, \vec{t}_k + \frac{\delta}{2}\right) \\ k_3 &= f\left(\vec{x}_k + k_2 \frac{\delta}{2}, \vec{u}_k, \vec{t}_k + \frac{\delta}{2}\right) \\ k_4 &= f\left(\vec{x}_k + \delta, \vec{u}_k, \vec{t}_k + \delta\right) \\ \vec{x}_{k+1} &= \vec{x}_k + \frac{\delta}{6}(k_1 + 2k_2 + 2k_3 + k_4) \\ &\qquad \text{for } k = 0, 1, \ldots, n-1. \end{aligned} \tag{22}$$

A fixed-step-size method is chosen for this integration because adaptive methods often belabor the process in the face of noisy data.

Process noise is applied to the user input force and gravity compensation torques to help compensate for noisy force readings and modeling inaccuracies in (16). The process noise covariance Q_k is then a 4×4 diagonal matrix. Each element of Q_k was tuned until a satisfactory balance between noise rejection and parameter convergence was achieved (results shown in Table IV). In general, the UKF performs better with slightly higher process noise, which opens up the filter by decreasing

TABLE IV
PROCESS NOISE COVARIANCE VALUES

Q(1)=5 N^2	Q(2)=5 N^2
Q(3)=5 N^2	Q(4)=10N^2m^2

TABLE V
SENSOR NOISE VARIANCES

	Θ	ϕ	r
q	30 μrad^2	70 μrad^2	2 μm^2
$\dot{q}$	7 mrad^2/s^2	8 mrad^2/s^2	1 mm^2/s^2

the weight given to the parametric model. The diagonal values of Q_k are given in Table IV. The covariance of the measurement noise, R_k from (21), is chosen to be a diagonal matrix with the values found in Table V as its elements (see Section III-C for more detail on R_k).

The UKF uses sigma points to propagate the covariance through the nonlinear dynamics. These sigma points are deterministic samples of the state defined by a weighting and the current error covariance. The distribution, scaling, and weighting of the sigma points are manipulated with three parameters: $\alpha, \beta,$ and κ. Here, these parameters were chosen as 0.5, 2, and 2, respectively, based on [26]. These values allow the UKF to capture a probability distribution up to its sixth moment.

C. Data Acquisition and Sensing

The BAM is controlled through a custom software application developed that can handle all sensor information. The spherical axes have quadrature encoders, and the handle is equipped with a 6-DOF force/torque sensor. These sensors are placed as close as possible to the user's point of interaction. The force, position sensing, and haptic renderings are updated at a rate of 2 kHz. Data recording, for postprocessing, occurs concurrently at a lower frequency, ∼500 Hz; this helps to reduce file size and increase program efficiency. Before entering the control loop, force signals are sent through a digital low-pass finite-impuse response (FIR) filter with an invariant delay of 25 ms that is designed to attenuate noise over 20 Hz. The joint velocities are calculated with a 20-MHz clock, in hardware on the DAQ board, by feeding a counter's gate each pulse train from the optical encoders. The counter in turn generates a frequency measurement. This frequency is scaled by the encoder resolution resulting, in angular velocity. Velocity measurement in this manner provides a clear signal that is devoid of timing inconsistencies imposed by the windows operating system [27]. A diagram depicting the data flow is shown in Fig. 5.

Both position and velocity measurements are susceptible to noise from half-read encoder ticks, vibrations, or imperfections/misalignment in the encoder wheel. To estimate the noise of the position/velocity measurements, the BAM's yaw, pitch, and extension were commanded to their locked state, and the endpoint was vibrated to induce jitter in the encoder readings over a 10-s length of time. The data were recorded and variance was calculated from that data. It should be noted that the measurement noise is not strictly Gaussian, because its magnitude

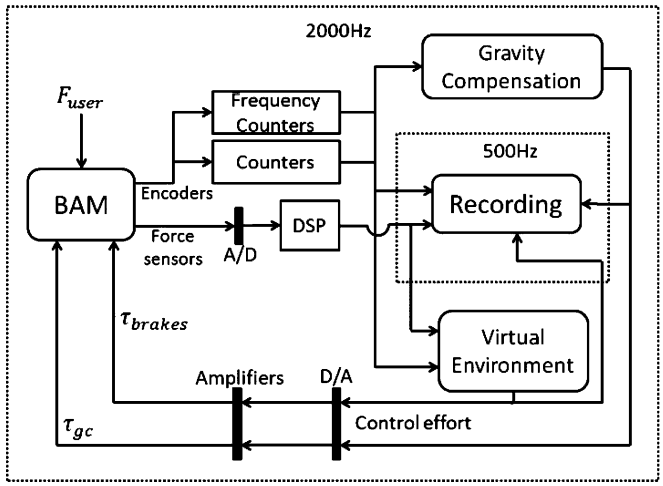

Fig. 5. Schematic of sensor/actuator configuration and control loop.

and frequency depend on the velocity/position and condition of the encoder. However, we approximate this noise as Gaussian. The variances from the experiment are listed in Table V and play a role in tuning the UKF.

Force sensing is done with two pairs of Nano25 six-axis force sensors (ATI-IA, Apex, NC) Four sensors are used to distribute the large user force and decrease strain on each sensor. The four sensors' data are used in parallel to reconstruct the input force vector in three dimensions. Since it is impossible to exert a torque on the force sensors with the 3-DOF handle, the torque information is currently unused. The force sensors were individually calibrated before being mounted on the BAM; however, the strain gauges inside the sensors tend to have some variance associated with their "no load" readings, hence injecting noise into the system. To combat this issue, a "tare" function was implemented. This function averages all force signal levels on startup, and then zeros the readings. The handle's weight imposes extraneous loadings on the sensors before any measurements are even recorded, and thus, $\vec{f}_{\text{user}}$ from (19) is augmented by the handle weight W_h (12.5 N)

$$\vec{f}_{\text{user}} = \begin{bmatrix} f_{\text{user},x} \\ f_{\text{user},y} - W_h(1-\cos(\phi)) \\ f_{\text{user},z} + W_h \sin(\phi) \end{bmatrix} \tag{23}$$

where $f_{\text{user},i}$ is the user force orthogonal to the end-effector. The noise present on the force sensor is most likely correlated across its axes, due to electrical and mechanical coupling of the strain elements through sensor parallelism. For the purposes of this paper, the noise is assumed to be Gaussian zero mean.

IV. SYSTEM IDENTIFICATION RESULTS

Fig. 6 shows the trajectory chosen as the input that contains varying frequency and amplitude producing motion about all three axes. This input is meant to reflect a nominal use of the device in a virtual environment.

The UKF is applied to the data collected from this input trajectory. The filter results in smoothed position and velocity estimates accompanied by their covariance. The 99% confidence

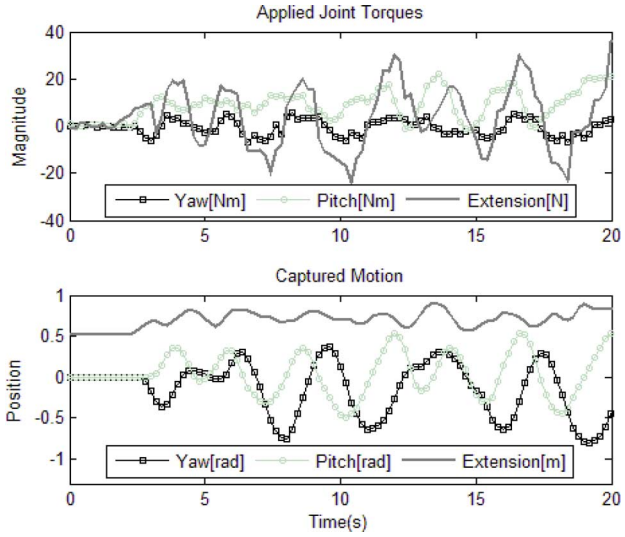

Fig. 6. (Top) Resulting joint torques from user input and gravity compensation used to carry out the system identification. (Bottom) Overall device motion.

TABLE VI
UKF POSITION AND VELOCITY ERROR—3σ BOUNDS

	Θ	ϕ	r
q	2.8 mrad	5.2 mrad	0.9 mm
$\dot{q}$	43 mrad/s	62 mrad/s	19 mm/s

level bounds for position and velocity prediction are shown in Table VI. The position state estimates are virtually the same as their experimental counterparts, and the velocity measurements are also tracked extremely well by the UKF. These clean results were expected because the measurement noise covariance R_k was very small due to highly accurate sensors.

The UKF has been configured to produce parameter estimates concurrently with state estimates. Fig. 7 shows the time course of parameter convergence. Initially, startup transients can be seen, but the filter is able to lock onto a stationary value within the first 10 s. The damping, friction, and inertia estimates are found in Table VII.

To validate the parameter estimates of the UKF, we implemented a virtual environment, with open-loop control, to produce a viscous field with constant damping (40 Ns/m) along the *X*, *Y*, and *Z* directions in the Cartesian frame. The joint damping coefficients were calculated as, $K_d = J^T K_{d,xyz} J$, where the expanded state matrix from Table III was changed to estimate damping in Cartesian space. Initial conditions, inertia, and friction estimates for this experiment were unchanged. Fig. 8 shows the time course of the damping estimate convergence in a viscous field.

V. VALIDATION AND DISCUSSION

A. *Analysis of Friction, Damping, and Inertia Estimates*

The estimation processes have provided insight into the physical workings of the BAM that is critical for controlling a user's movements.

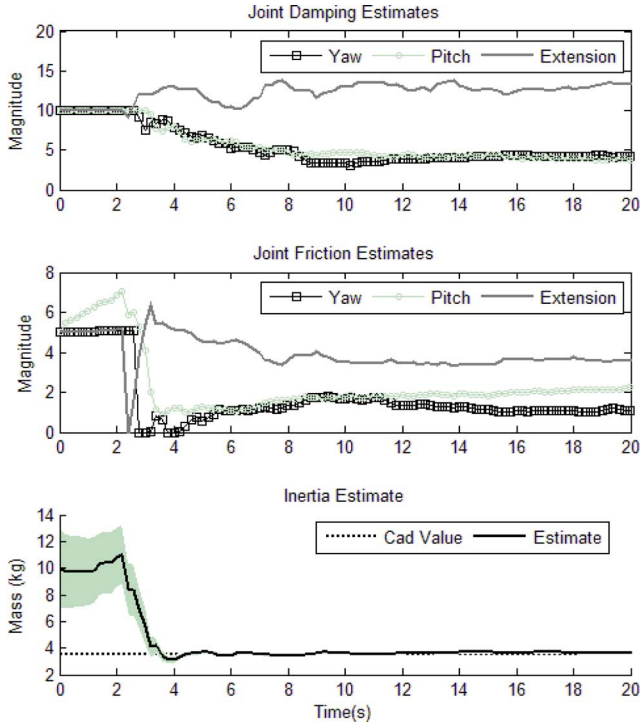

Fig. 7. (Top) Joint viscous damping parameters. (Middle) Friction estimates for each axis. (Bottom) Estimated prismatic joint inertia with confidence bounds and CAD estimate.

TABLE VII
PARAMETER VALUES AND STANDARD ERRORS FROM THE UKF

Parameter	Estimate (σ)
$K_{d\theta}$ [Nms^2/rad]	4.17 (0.128)
$F_{c\theta}$ [Nm]	1.086 (0.103)
$K_{d\phi}$ [Ns^2/m]	3.75 (0.296)
$F_{c\phi}$ [Nm]	2.25 (0.109)
K_{dr} [Ns/m]	13.37(0.427)
F_{cr} [N]	3.57(0.103)
m [kg]	3.552(0.0132)

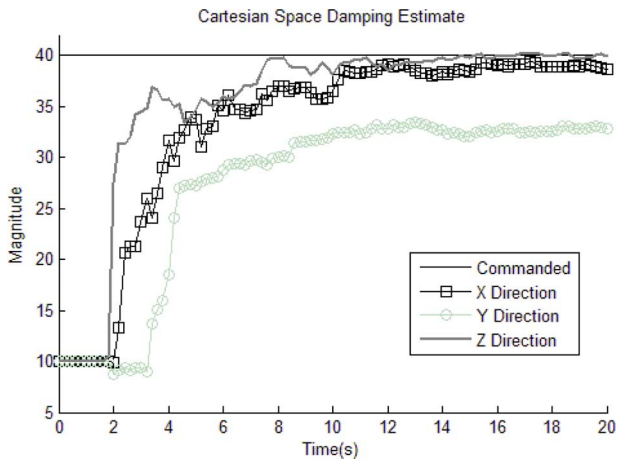

Fig. 8. Convergence of Cartesian damping estimates during a movement through a viscous field environment.

The joint damping estimates for the pitch and yaw axes share an identical transmission construction and converge to statistically indifferent values, whereas the prismatic joint converges to a higher overall damping due to its belt drive. The prismatic joint's friction is higher than the rotational joints due to nylon rollers. The pitch and yaw friction values are similar, but the pitch has a higher friction that is likely from friction in the gravity compensator or discrepancies between cable tensions in the transmission.

The UKF estimate for the extension arm inertia is within the 95% confidence interval for the mass extracted from CAD in Section II. Another validation comes from Fig. 8, where a desired damping was controlled open-loop based on noisy velocity measurements. The UKF is able to track the fact that the system's overall damping has changed and demonstrates the robustness of the algorithm toward its initial conditions. The Z-direction damping (primarily prismatic joint motion) is not significantly different than the commanded value ($p < 0.05$). Examining the same damping estimates for the X and Y directions (primarily yaw and pitch), we see that indeed the mechanical structure of the BAM is affecting the behavior of what is meant to be experienced in the viscous virtual environment.

B. Force Estimation Through Inverse Dynamic Model

The device parameters are estimated to design better controllers and more accurately estimate user interactions with the device during rehabilitation. Often, the user's force is the quantity to be controlled, and the prediction of this value without sensors benefits cost, complexity, and weight. To this end, we compared measured forces against estimated user force from an inverse dynamic model using the parameters from Tables II and VII. The results are shown in Fig. 9, both with and without the frictional effects incorporated into the models.

The most striking feature of Fig. 9 is how dramatic the effect of friction is for each joint. The simple viscous plus Coulomb model of (20) allows the force prediction to closely follow the input for all three axes simultaneously. The error in the pitch axis between 6 and 8 s is attributed to the gravity compensation mechanism catching up to a large step input from the extension axis. Small jitters observed in the force estimates are in part due to ripple in filtered velocity and the effect of friction at velocities that are close to zero.

C. Future Online UKF Implementation

When the virtual environment is switched on and intended to produce some desired effect, such as damping, we have no way of directly measuring this quantity. In the future, we plan to implement an online version of the UKF to monitor and further refine the desired effect. The computational complexity of the UKF could hinder the performance of any software running it in real time. To combat this, few methods may be employed. First, because the measurement noise is linearly additive, a simpler algorithm for the UKF can be constructed [11] to reduce the size of the full augmented state. Second, the main bottleneck in the algorithm, which is taking a matrix square root of the error covariance to calculate the sigma points, can be simplified. The matrix square root is accomplished with Cholesky decomposition, but implementing a "square root" version of the UKF eliminates this operation by propagating the square root of the covariance through the dynamics instead, increasing performance by up to 20% [28].

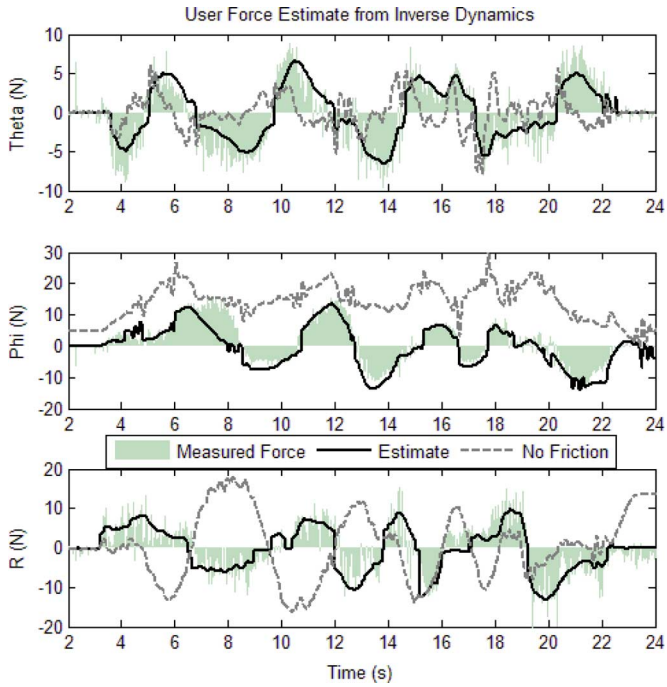

Fig. 9. Plots show user's force with predictions of force from the inverse dynamic model with and without friction terms. The effect of friction is dramatic along all axes, but the model shows good agreement with ground truth.

D. Comparison With Other Haptic Devices Used in Rehabilitation Research

In light of the results presented here, we chose to compare the BAM against the largest workspace commercially available haptic devices used for rehabilitation research. Three haptic devices have been chosen: the large-workspace Phantom 3.0 (Sensable, Woburn, MA) [1], an admittance-controlled device with spherical kinematics, the HapticMaster (MOOG-FCS, Ann Arbor, MI) [4], and the DHD (Force Dimension, Switzerland) [2]. These comparisons are meant to give the reader a feel for the inertial, frictional, and force production characteristics of a brake-actuated system versus common motor driven devices; they are outlined in Table VIII.

The BAM is an electrically efficient device consuming less power than a 60-W light bulb, yet maintaining high force levels and a large workspace. The BAM's workspace, in comparison, is the largest of the four by as much as 28 times. The Phantom 3.0 has the second largest workspace, but its maximum torque is only 22 N, which is less than one tenth of the BAM's capability for continuous maximum torque with braked actuation. For rehabilitation paradigms, we need to have a device that is able to continuously resist a large amount of force, and the BAM is suitable for these tasks.

TABLE VIII
HAPTIC DEVICE PERFORMANCE COMPARISON

	BAM	Haptic Master	Phantom 3.0	DHD
Work space	$\sim 2m^3$	$\sim 0.08m^3$	$\sim 0.2m^3$	$\sim 0.07m^3$
Max. force	134N	110N	22N	20N
Stiffness	2 to 108 $\frac{kN}{m}$	10 to 50 $\frac{kN}{m}$	1 $\frac{kN}{m}$	14.5 $\frac{kN}{m}$
Friction	0.6 to 3N	0.01N	0.2N	unlisted
Min. tip inertia	3.56kg	2kg	0.22kg	unlisted
Position resolution	240μm 375 to 785μrad	4 to 12 μm	20μm 40 to 140μrad	10μm 698μrad

In terms of inertia, the Phantom has the lowest reported value, with a significant compromise on the device stiffness. The HapticMaster and BAM both incorporate prismatic joints, which unfortunately add inertia. The BAM's inertia is 1.78 times larger than the HapticMaster; however, 1.78 is small, considering that the BAM's workspace is 25 times larger than the HapticMaster's.

For stiffness, the DHD can produce higher stiffness compared to the Phantom, due to its parallel kinematic construction, but the BAM is capable of producing stiffer and harder constraints without questions of controller stability because it is, by definition, a passive device.

Viscous friction values were not reported, or are nearly zero for the three other devices placing the BAM in last place regarding minimum force resolution. Considering the overall size of our device, the frictional effects are negligible for gross motion, weakly impacting our force rendering ability.

Overall, in this comparison, it is clear that the performance of each of the four devices is high for different task requirements. The HapticMaster, Phantom, and DHD are better suited to wrist and forearm manipulation in small or mobile environments that require high resolution of control within that space. However, the BAM redefines the notion of a "large workspace" device, offering a new haptic environment for *safer* whole-limb life-size exploration, permitting strong interaction force for strength building, and creating more realistic rehabilitation paradigms related to activities of daily living impossible with other devices. These differences highlight the enhanced safety and stability of braked actuation.

E. Conclusion

We designed and constructed the 6-DOF BAM, and modeled and identified the system parameters using unscented Kalman filtering. In particular, we demonstrated how general human input can be used for system identification of passive devices, and how these estimated parameters allow accurate controls for haptic interactions. It is clear that larger devices such as the BAM are needed in the space of rehabilitation, and the safety issues need to be addressed. We are currently improving multiple facets of the device by miniaturizing the mechanisms, creating controllers to provide smooth path guidance [29], incorporating a head-mounted display to accommodate virtual environments (including a large peripheral environment), and using visual feedback distortion to extend the ability of brake-actuated devices [30]. In the future, we hope to show the BAM as an invaluable tool for whole-limb rehabilitation in clinical and domestic contexts.

REFERENCES

[1] PHANToM Premium 3.0 Haptic Device, Sensable Technologies, Inc. (2009). [Online]. Available: http://www.sensable.com

[2] Delta Haptic Device, Force Dimension. (2009). [Online]. Available: http://www.forcedimension.com

[3] WAM robot, Barrett Technology, Inc. (2009). [Online]. Available: http://www.barett.com

[4] R. Q. Van Der Linde, P. Lammertse, E. Frederisksen, and B. Ruiter, "The HapticMaster, a new high-performance haptic interface," in *Proc. Eurohaptics*, Edinburgh, U.K., 2002, pp. 1–5.

[5] P. S. Lum, C. G. Burgar, and H. F. M. Van Der Loos, "The use of a robotic device for post-stroke movement therapy," in *Proc. Int. Conf. Rehabil. Robot.*, Bath, U.K., Apr. 14–15, 1997.

[6] R. Loureiro, F. Amirabdollahian, S. Coote, E. Stokes, and W. Harwin, "Using haptics technology to deliver motivational therapies in stroke patients: Concepts and initial pilot studies," in *Proc. Eurohaptics*, Birmingham, U.K., 2001, pp. 1–6.

[7] J. E. Colgate, W. Wannasuphoprasit, and M. A. Peshkin, "Cobots: Robots for collaboration with human operators," in *Proc. IMECE*, 1996, pp. 433–439.

[8] D. K. Swanson and W. J. Book, "Path-following control for dissipative passive haptic displays," in *Proc. 11th Symp. Haptic Interfaces Virtual Environ. Teleoperator Syst.*, 2003, pp. 101–108.

[9] Y. Matsuoka and W. T. Townsend, "Design of lifesize haptic environments," in *Experimental Robotics VII*, D. Rus and S. Singh, Eds. London, U.K.: Springer-Verlag, 2001, pp. 461–470.

[10] T. Rahman, R. Ramanathan, R. Seliktar, and W. Harwin, "A simple technique to passively gravity-balance articulated mechanisms," *ASME Trans. Mech. Des.*, vol. 117, no. 4, pp. 655–658, 1995.

[11] M. R. Reed and W. J. Book, "Modeling and control of an improved dissipative passive haptic display," in *Proc. IEEE Int. Conf. Robot. Autom.*, 2004, vol. 1, pp. 311–318.

[12] J. An and D. Kwon, "In haptics, the influence of the controllable physical damping on stability and performance," in *Proc. IEEE Int. Conf. Intell. Robots Syst.*, 2004, vol. 2, pp. 1204–1209.

[13] K. Salisbury, W. Townsend, B. Ebrman, and D. DiPietro, "Preliminary design of a whole-arm manipulator system (WAMS)," in *Proc. IEEE Int. Conf. Robot. Autom.*, 1988, vol. 1, pp. 254–260.

[14] C. Iurian, F. Ikhouane, J. Rodellar, R. Grino, and I. Cubero, "Identification of a system with dry friction," Inst. d'Org. i Control de Sistemes Ind., Univ. Politècnica de Catalunya, Barcelona, Spain, Tech. Rep., 2005.

[15] C. Richard, M. R. Cutkosky, and K. MacLean, "Friction identification for haptic display," in *Proc. ASME, Dyn. Syst. Control Div.*, 1999, vol. 67, pp. 327–334.

[16] A. M. Tahmasebi, B. Taati, F. Mobasser, and K. Hashtrudi-Zaad, "Dynamic parameter identification and analysis of a PHANToM haptic device," in *Proc. IEEE Conf. Control Appl.*, 2005, pp. 1251–1256.

[17] A. Janot, C. Bidar, F. Gosselin, M. Gautier, D. Keller, and Y. Perrot, "Modeling and identification of a 3 DOF haptic interface," in *Proc. IEEE Int. Conf. Robot. Autom.*, 2007, pp. 4949–4955.

[18] G. Calafiore, M. Indri, and B. Bona, "Robot dynamic calibration: Optimal excitation trajectories and experimental parameter estimation," *J. Robot. Syst.*, vol. 18, no. 2, pp. 55–68, 2001.

[19] J. L. Crassidis and J. L. Junkins, *Optimal Estimation of Dynamic Systems*. London, FL, U.K./Boca Raton FL: Chapman & Hall/CRC, 2004.

[20] S. Tam, E. Kubica, and D. Wang, "A system identification technique for haptic devices," in *Proc. IEEE Conf. Control Appl.*, 2005, pp. 1240–1245.

[21] S. F. Masri, A. G. Chassiakos, and T. K. Caughey, "Structure-unknown non-linear dynamic systems: Identification through neural networks," *Smart Mater. Struct.*, vol. 1, pp. 45–56, 1992.

[22] A. Gretton, A. Doucet, R. Herbrich, P. J. W. Rayner, and B. Scholkopf, "Support vector regression for black-box system identification," in *Proc. IEEE Signal Process. Workshop Statist. Signal Process.*, 2001, pp. 341–344.

[23] M. Blauer and P. R. Belanger, "Signal and parameter estimation for robotic manipulators using force measurements," *IEEE Trans. Automat. Control*, vol. AC-32, no. 12, pp. 1067–1075, Dec. 1987.

[24] E. A. Wan and R. V. D. Merwe, "The unscented Kalman filter for nonlinear estimation," in *Proc. IEEE Adaptive Syst. Signal Process., Commun., Control Symp.*, 2000, pp. 153–158.
[25] S. J. Julier, J. K. Uhlmann, and H. F. Durrant-Whyte, "A new approach for filtering nonlinear systems," in *Proc. Amer. Control Conf.*, 1995, vol. 3, pp. 1628–1632.
[26] S. Thrun, W. Burgard, and D. Fox, *Probabilistic Robotics*. Cambridge, MA: MIT Press, 2005.
[27] T. Laopoulous and C. Papageorgiou, "Microcontroller-based measurement of angular position velocity and acceleration," in *Proc. IEEE Instrum. Meas. Conf.*, 1996, pp. 73–77.
[28] R. Van Der Merwe and E. Wan, "The square-root unscented Kalman filter for state and parameter estimation," in *Proc. Int. Conf. Acoust., Speech, Signal Process.*, 2001, pp. 3461–3464.
[29] B. Dellon and Y. Matsuoka, "Path guidance control for a safer large scale dissipative haptic display," in *Proc. IEEE Int. Conf. Robot. Autom.*, 2008, pp. 2073–2078.
[30] B. Dellon and Y. Matsuoka, "Feedback distortion to augment controllability of human limb motion," in *Proc. Virtual Rehabil.*, 2008, pp. 22–27.

Brian Dellon received the B.S. and M.S. degrees (with university honors) in 2005 and 2007, respectively, from Carnegie Mellon University, Pittsburgh, PA, where he is currently working toward the Ph.D. degree in mechanical engineering.

Mr. Dellon was elected to the Tau Beta Pi and Pi Tau Sigma honor societies.

Yoky Matsuoka (M'03) received the B.S. degree from the University of California, Berkeley, in 1993, and the M.S. and Ph.D. degrees from Massachusetts Institute of Technology, Cambridge, in 1995 and 1998, respectively, all in electrical engineering and computer science.

She is currently an Associate Professor of computer science and engineering with the University of Washington, Seattle.

Dr. Matsuoka received the Presidential Early Career Award for Scientists and Engineers in 2004, the Anna Loomis McCandless Chair in 2004, the IEEE Robotics and Automation Society Early Academic Career Award in 2005, and the MacArthur Fellowship in 2007.